

Full length article

Spectral TRIP enables ductile 1.1 GPa martensite

M.-M. Wang^a, C.C. Tasan^{b,*}, D. Ponge^a, D. Raabe^a^a Max-Planck-Institut für Eisenforschung, Max-Planck-Straße 1, 40237 Düsseldorf, Germany^b Department of Materials Science and Engineering, Massachusetts Institute of Technology, 77 Massachusetts Avenue, Cambridge, MA 02139, USA

ARTICLE INFO

Article history:

Received 31 July 2015

Received in revised form

25 March 2016

Accepted 28 March 2016

Available online 6 April 2016

Keywords:

Martensitic transformation

Twinning

Grain size

ECCI

Medium manganese steel

ABSTRACT

Introduction of interlath reverted austenite is an effective method to design ductile lath martensitic steels. The challenge in this concept is that all reverted austenite films have similar mechanical stability, hence, they all undergo transformation-induced plasticity (TRIP) at the same strain level. Here we propose a new thermo-mechanical treatment route to activate the TRIP effect over a broad strain regime and refer to it as 'spectral TRIP effect'. It aims at spreading the micro-mechanical stability of reverted austenite grains by widening the austenite nucleation barrier in martensite. To validate the proposed thermo-mechanical treatment route, an as-quenched medium-Mn martensitic steel was cold rolled prior to the reversion treatment at 600 °C. Microstructure characterization was carried out by electron backscatter diffraction (EBSD) and electron channeling contrast imaging (ECCI). Mechanical tests show that the approach is effective. The spectral TRIP effect improves both, the strength and the ductility due to the well dispersed size distribution and the associated size-dependent deformation and phase transformation behavior of the reverted austenite grains, extending TRIP-related work hardening over a broad strain range.

© 2016 Acta Materialia Inc. Published by Elsevier Ltd. All rights reserved.

1. Introduction

The challenge that we address in this work is to design ductile martensitic steels [1–3]. In a previous study, we demonstrated that after reversion treatment of a lath martensitic steel (Fe–9Mn–3Ni–1.4Al–0.01C, mass%), the resultant nanolaminate microstructure consisting of alternating layers of martensite and reverted austenite exhibits enhanced ductility and toughness with maintained ultimate tensile strength compared to the non-heat treated material [4]. This improvement in properties was linked to the dynamic nature of the strain partitioning between the martensite and reverted austenite phases, which itself arises due to a size dependent competition between mechanically-induced martensitic transformation and mechanical twinning mechanisms in austenite [5,6]. Here, we develop this basic approach further by systematically exploiting this size dependence, thus extending the associated TRIP-related work hardening over a broader strain range for simultaneously improving both, the material's strength and ductility.

Note that, the dispersion of the TRIP effect of retained/reverted

austenite has been the core microstructure design challenge for enhancing the strain hardening ability and ductility of multiphase TRIP steels [7–9], medium-Mn steels [10–12], and quench & partitioning steels [13–15], etc. Majority of present efforts include large-matrix experimental programs, providing wide range screening of different chemical compositions or thermo-mechanical treatments for their effects on mechanical properties [10–12,16,17], whereas few dig deeper into a certain thermo-mechanical route to better connect properties to changes in the microstructure [18,19]. Our goal here is to identify an optimal thermo-mechanical pathway and explore its micro-mechanical consequences in detail to identify its full potential to successfully address this design challenge.

The microstructure design strategy is as follows: To achieve a wider austenite grain size distribution, it is required to introduce a correspondingly wider distribution of potential nucleation sites for austenite in the martensite microstructure, e.g. a range of sites with different nucleation energy barriers. The nucleation energy barrier associated with the reversion of martensite to austenite consists of three energy components [20–24], namely, the change in chemical free energy, interface energy and elastic misfit energy. The first energy component, i.e. the change in free energy, arises from the difference in chemical composition and atomic arrangements

* Corresponding author.

E-mail address: tasan@mit.edu (C.C. Tasan).

between the martensite matrix and the austenite reversion nucleus [22]. The second term, i.e. the change in interface energy, is determined by the net interface energy differences between the original martensite/martensite grain boundary, the newly formed martensite/austenite interface and the austenite/austenite interface (if an internal boundary exists inside the nucleus) [24]. The final energy component, i.e. the change in elastic energy, is the gain in elastic energy since the highly elastically strained martensite is replaced by the austenite nucleus [24]. In certain cases, when the reversion proceeds via displacive mechanism, elastic misfit stresses must be considered between the two phases [25–28].

In the current reversion treated lath martensite, it is shown that (i) the reversion of martensite to austenite is a reconstructive process controlled by diffusion and the reverted austenite grains contain minor amounts of stacking faults (SFs); and (ii) the reverted austenite and the abutting host martensite exhibit a K–S (Kurdjumov–Sachs) orientation relationship at least along one interface. Thus, the decisive parameter in introducing a wider spectrum of differences in nucleation energy lies in controlling the energy associated with the martensite grain boundaries, since nucleation along high angle martensite grain boundaries would lead to high gain in both interface energy and elastic energy.¹ It follows then that modifying the misorientation distribution of martensite grain boundaries should efficiently lead to a diversification of the nucleation sequence for reverted austenite, enabling a spectral TRIP effect.

In this context, the benefits of imposing cold deformation to the martensite prior to the reversion treatment are worth considering. Cold deformation introduces various defects that can act as nucleation centers for reversion, namely, grain boundaries with a wide range of misorientations, shear bands, lamellar boundaries containing geometrically necessary dislocations, and cell boundaries with statistically distributed dislocations [29–33]. Processing benefits also exist: steel sheet products always require some degree of rolling for reducing their thickness and enabling kinetics of the involved process, e.g. accomplishment of transformation processes during subsequent annealing.

These considerations motivated us to investigate the potential of cold rolling as a means of adjusting the nucleation barrier for austenite, by introducing a wide distribution of internal boundaries. In the following, first the influence of cold rolling on the martensite microstructure and the subsequential austenite reversion process are presented. Then the mechanical properties of the reversion-treated cold-rolled martensite are examined and the microstructure evolution during deformation is mapped and discussed in the light of earlier observations [4,5]. Finally, the relationship between the microstructure and the mechanical properties in reversion-treated cold-rolled martensite is discussed and conclusions are drawn.

2. Experimental procedure

The starting material is a TRIP-maraging steel with nominal chemical composition of Fe–9Mn–3Ni–1.4Al–0.01C (mass %) [4,5,24,34,35]. The metallurgical and thermo-mechanical processes to produce a steel plate (~5 mm) with an as-quenched α' martensite microstructure are described elsewhere [5]. The as-quenched steel

plate was cold rolled from ~5 mm to ~1.5 mm (~70% thickness reduction). Partial reversion of cold-rolled α' martensite to austenite (γ) was carried out at 550 °C, 575 °C and 600 °C for short periods (10 min, 30 min or 1 h) and then quenched in water. Uniaxial tensile tests with initial strain rate of 10^{-3} s^{-1} were conducted for selected aging conditions combined with digital image correlation (DIC) using Aramis software (GOM GmbH) [36,37]. Microstructures were characterized by scanning electron microscopy (SEM) based electron backscatter diffraction (EBSD), electron channeling contrast imaging (ECCI) and secondary electron imaging (SE imaging) analysis. Details of the sample preparation protocols and microstructure characterization parameters can be found in Ref. [5].

3. Results

3.1. Microstructure evolution during processing

Table 1 introduces the naming convention for characterizing the different deformation and heat treatment states: In what follows, based on the starting state of the microstructure (as-quenched: AQ, cold-rolled: CR), the annealing time at 600 °C and the microstructural constituents (martensite: M, austenite: A) samples are named as listed in Table 1.²

The as-quenched and the cold-rolled microstructures are characterized by light optical micrographs and EBSD phase maps in conjunction with an overlay of the image quality maps in Fig. 1. In the as-quenched state $M_{(AQ)}$, the microstructure consists of an α' martensite phase matrix (phase in red) (Fig. 1a₂) and various types of boundaries in the microstructure including prior austenite grain boundaries as well as martensite packet/block/lath boundaries (Fig. 1a₁) [38,39]. After cold rolling, the deformed microstructure (sample state $M_{(CR)}$) is characterized by a α' martensite matrix with numerous deformation bands, as indicated by white color arrows in Fig. 1b₁–b₂.

The influence of cold rolling on the distribution of the internal interfaces in the microstructure is shown in Fig. 2. The distributions of grain boundaries in as-quenched martensite $M_{(AQ)}$ and cold-rolled martensite $M_{(CR)}$ are plotted in Fig. 2a₁ and b₁, respectively, where grain boundaries with 2°–15° misorientations, e.g. low angle grain boundaries, are in blue, and grain boundaries with 15°–62.8° misorientations, e.g. high angle grain boundaries, are in red.³ Compared to the as-quenched state $M_{(AQ)}$ (Fig. 2a₁), cold-rolled martensite $M_{(CR)}$ contains not only a higher density, but also a wider spatial distribution of high angle and low angle martensite grain boundaries (Fig. 2b₁). The difference in density and spatial distribution of martensite grain boundaries can be clearly seen by comparing the two magnified images shown in Fig. 2a₂ and b₂, and the martensite grain boundary distribution in Fig. 2c.

The influence of the density and distribution of the martensite grain boundaries on the subsequential γ reversion process at 600 °C is presented in Fig. 3. It shows the EBSD phase maps for sample states $M-A_{(AQ+1h)}$, $M-A_{(AQ+4h)}$ and $M-A_{(AQ+8h)}$ (Fig. 3a₁–a₃), phase maps (Fig. 3b₁–b₃) and γ phase size maps (Fig. 3c₁–c₃) for states $M-A_{(CR+10min)}$, $M-A_{(CR+30min)}$ and $M-A_{(CR+1h)}$. In the γ phase size maps, each grain is color coded (from blue to red, rainbow code) by its

¹ This was already observed in our previous work [4]: during the short time annealing of as-quenched martensite at 600 °C, reverted austenite grains were mainly formed along prior austenite grain boundaries and martensite packet/block boundaries, i.e. both are types of interfaces with high misorientations and energies. With longer annealing time, reverted austenite grains are also formed along martensite lath boundaries, i.e. grain boundaries with low misorientations.

² To exclude the influence of aging temperature on austenite reversion kinetics and chemical composition of reverted austenite, results of microstructure characterizations and mechanical tests are only presented here for aging treatments at 600 °C. But note that sufficient tests, e.g. microstructure characterizations of eight different aging treatments and mechanical testing of four aging conditions, were carried out to confirm the proposed thermo-mechanical treatment route.

³ 62.8° is the maximum misorientation between two cube crystals [68].

Table 1

Sample abbreviations based on the starting state of the microstructure (as-quenched: AQ, cold-rolled: CR), the annealing time at 600 °C and the microstructural constituents (martensite: M, austenite: A).

Annealing time @ 600 °C	Microstructure prior to reversion annealing	
	As-quenched martensite [4,5]	Cold-rolled martensite [this work]
0 min	$M_{(AQ)}$	$M_{(CR)}$
10 min		$M-A_{(CR+10min)}$
30 min		$M-A_{(CR+30min)}$
1 h	$M-A_{(AQ+1h)}$	$M-A_{(CR+1h)}$
4 h	$M-A_{(AQ+4h)}$	
8 h	$M-A_{(AQ+8h)}$	

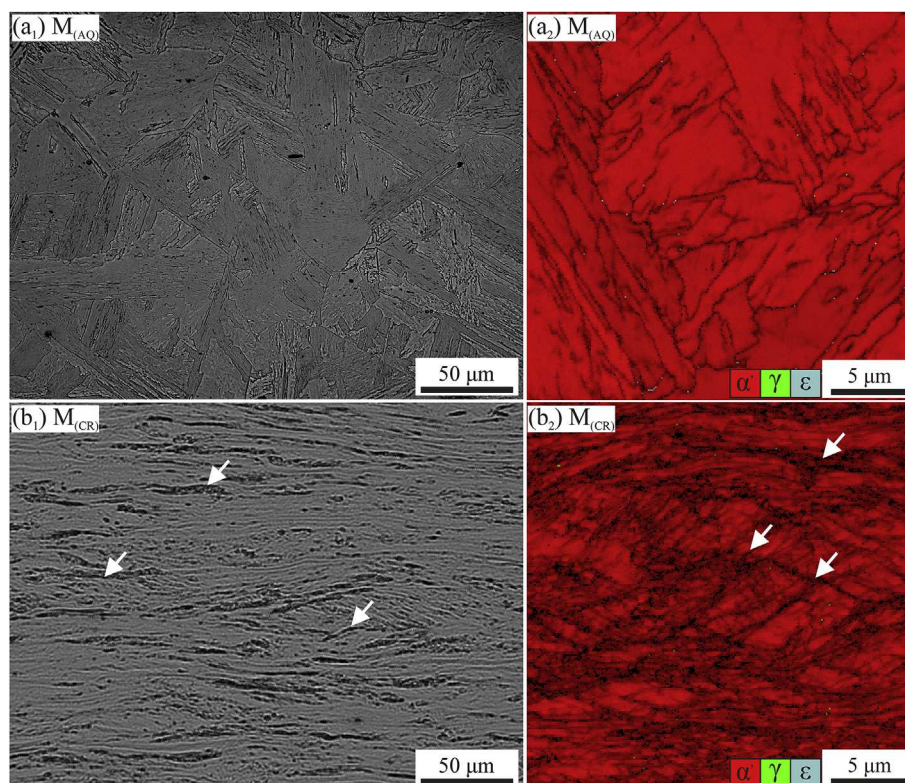


Fig. 1. Microstructure of (a) As-quenched martensite $M_{(AQ)}$; (b) Cold-rolled martensite $M_{(CR)}$, as characterized by (1) Light optical micrograph; (2) EBSD Phase map with an overlay of the EBSD image quality map.

grain size, e.g. γ grains in red are larger than those in blue.

For the as-quenched undeformed martensite, γ reversion takes place first along the martensite packet and block boundaries (see sample state $M-A_{(AQ+1h)}$ in Fig. 3a₁), then also along martensite lath boundaries (see sample state $M-A_{(AQ+4h)}$ in Fig. 3a₂). These initially nano-sized films of γ eventually grow thicker after 8 h annealing at 600 °C (see sample state $M-A_{(AQ+8h)}$ in Fig. 3a₃).

Due to the higher density and spatial distribution of martensite grain boundaries in cold-rolled martensite, a profoundly different γ reversion process is observed. Already after 10 min annealing at 600 °C, reverted γ grains are formed in the microstructure (see sample state $M-A_{(CR+10min)}$ in Fig. 3b₁). Comparing these with the distribution of the martensite boundaries observed in the cold-rolled state (Fig. 2b₁, b₂), it is clear that the reverted γ grains are preferentially formed along high angle martensite grain boundaries, e.g. at shear bands (see sample state $M-A_{(CR+10min)}$ in Fig. 3b₁). The preferred nucleation behavior of γ grains along high angle grain boundaries is consistent with the behavior observed in the as-quenched, i.e. undeformed martensite (Fig. 3a₁). During further

annealing of the cold-rolled martensite to 30 min, these γ grains which formed along high angle grain boundaries continue to grow while more γ grains are observed to newly nucleate along such grain boundaries which are characterized by lower angle misorientations (Fig. 2b₁, Fig. 3b₂). Due to the difference in nucleation sequences and thus time available for phase growth, γ grains that had formed along high angle grain boundaries assume a larger phase size than those formed along low angle grain boundaries (see sample state $M-A_{(CR+10min)}$ in Fig. 3c₁ and sample state $M-A_{(CR+30min)}$ in Fig. 3c₂). This process proceeds with further annealing. Eventually, after 1 h, the majority of the martensite grain boundaries are decorated by reverted γ grains (Fig. 3b₃, c₃). Comparing this state with the earlier sample states which were annealed for shorter times, i.e. $M-A_{(CR+10min)}$ (Fig. 3c₁) and $M-A_{(CR+30min)}$ (Fig. 3c₂), the reverted γ grains assume an overall larger grain size in the sample annealed for 1 h at 600 °C, i.e. $M-A_{(CR+1h)}$.

Thus, for both classes of samples, the as-quenched martensite and the cold-rolled martensite, high angle grain boundaries promote earlier nucleation of γ grains over low angle grain boundaries.

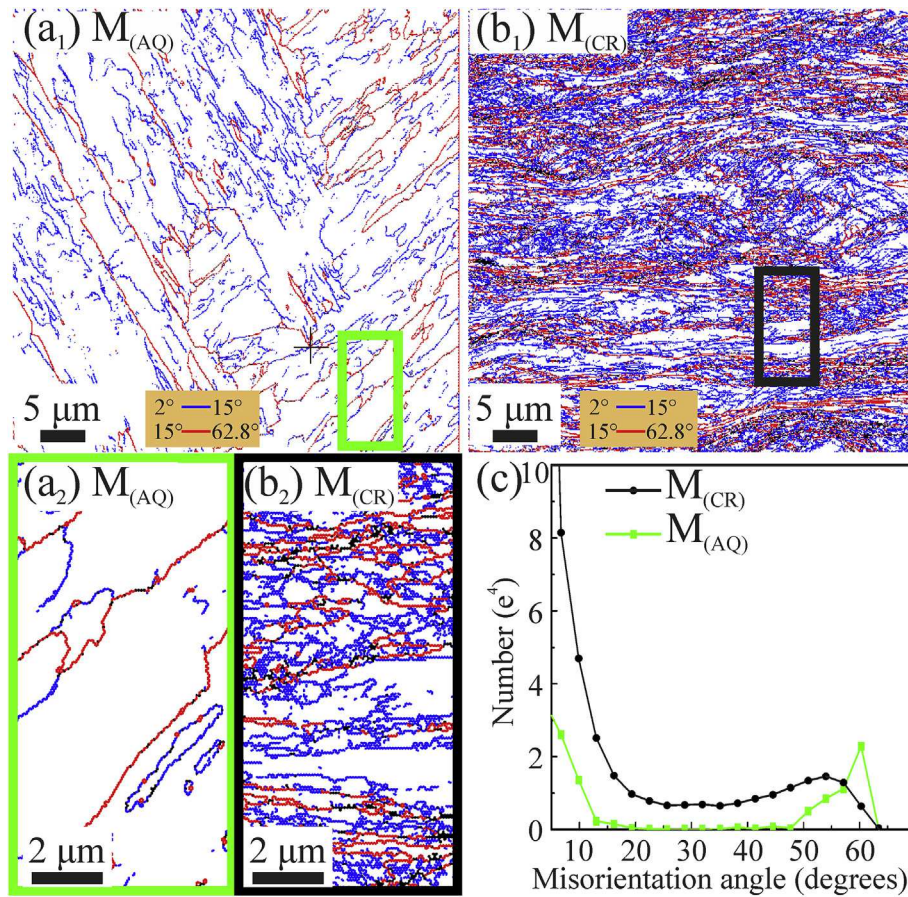


Fig. 2. Distribution of grain boundaries in (a₁, a₂) As-quenched martensite $M_{(AQ)}$; (b₁, b₂) Cold-rolled martensite $M_{(CR)}$, as characterized by EBSD measurements. (c) Quantified distribution of grain boundaries in as-quenched martensite $M_{(AQ)}$ and cold-rolled martensite $M_{(CR)}$.

Moreover, the high density and spatial distribution of high and low angle grain boundaries in cold-rolled α' martensite leads to a size distribution of γ grains after 1 h annealing at 600 °C.

Fig. 4a shows the influence of pre-straining of martensite on the γ reversion kinetics. We find that cold-rolled martensite $M_{(CR)}$ exhibits significantly faster γ reversion kinetics than as quenched martensite $M_{(AQ)}$, i.e. a higher γ fraction is observed for the former after the same annealing period at 600 °C. The size distribution of γ grains in sample $M-A_{(CR+1h)}$ is also quantified and plotted together with the width distribution of the γ nano-films in sample $M-A_{(AQ+8h)}$ in Fig. 4b. In sample $M-A_{(AQ+8h)}$, the majority of the γ grains have a width below 0.3 μm (green curve in Fig. 4b). In contrast, sample $M-A_{(CR+1h)}$ exhibits a broader γ grain size distribution (black curve in Fig. 4b). Thus, as planned, a broader size distribution of γ grains is successfully developed from the cold-rolled martensite.

3.2. Mechanical response

To assess whether the successfully realized microstructure design route positively enhances the mechanical properties as planned, the mechanical properties of the cold rolled and heat treated martensite sample $M-A_{(CR+1h)}$ are compared with those of the undeformed and heat treated sample $M-A_{(AQ+8h)}$ in Fig. 5. Sample $M-A_{(CR+1h)}$ exhibits a yield stress $\sigma_{0.2}$ of 870 MPa, ultimate tensile stress (UTS) of 1110 MPa, and uniform elongation (UE) of 17.1%, corresponding to 31% increase in $\sigma_{0.2}$, 23% increase in UTS and maintained UE value comparing with sample $M-A_{(AQ+8h)}$

(Fig. 5a). The DIC-based strain measurements also reveal that $M-A_{(AQ+8h)}$ and $M-A_{(CR+1h)}$ both exhibit substantial damage tolerance, i.e. comparable post-necking deformation capability, i.e. with similar amount of accumulated strain between the onset of the strain localization regime and failure.

The mechanical properties of sample $M-A_{(CR+10min)}$, $M-A_{(CR+30min)}$, $M-A_{(CR+1h)}$ and $M-A_{(AQ+8h)}$ are summarized in Fig. 5b. It is clear that after 1 h annealing of the cold-rolled martensite, sample $M-A_{(CR+1h)}$ exhibits improved mechanical properties compared to the 8 h annealed as-quenched undeformed martensite (sample $M-A_{(AQ+8h)}$). Thus, the proposed thermo-mechanical treatment route is proven to be effective.

Fig. 6a shows the strain hardening behavior for samples $M-A_{(AQ+8h)}$ and $M-A_{(CR+1h)}$. It is clear that $M-A_{(CR+1h)}$ (black curve in Fig. 6a) exhibits an enhanced strain hardening behavior during the later stage of deformation. Based on the strain hardening behavior presented in Fig. 6a, the deformation process of sample $M-A_{(CR+1h)}$ is divided into three stages, namely stage i - early uniform deformation regime ($\epsilon < 0.07$); stage ii - late uniform deformation regime ($0.07 < \epsilon < 0.14$); and stage iii - post-necking deformation stage ($\epsilon > 0.14$). To indicate the deformation and phase transformation behavior of the γ grains within these different deformation regimes shown in Fig. 6a, two datasets are plotted in Fig. 6b: (i) the kernel average misorientation (KAM) in γ (red data points); and (ii) the γ fraction (blue data points). The KAM parameter is the average misorientation of all neighboring points with respect to a given kernel (here 2nd neighbor, all points in kernel) [40]. To exclude the influence from neighboring grains or grain boundaries,

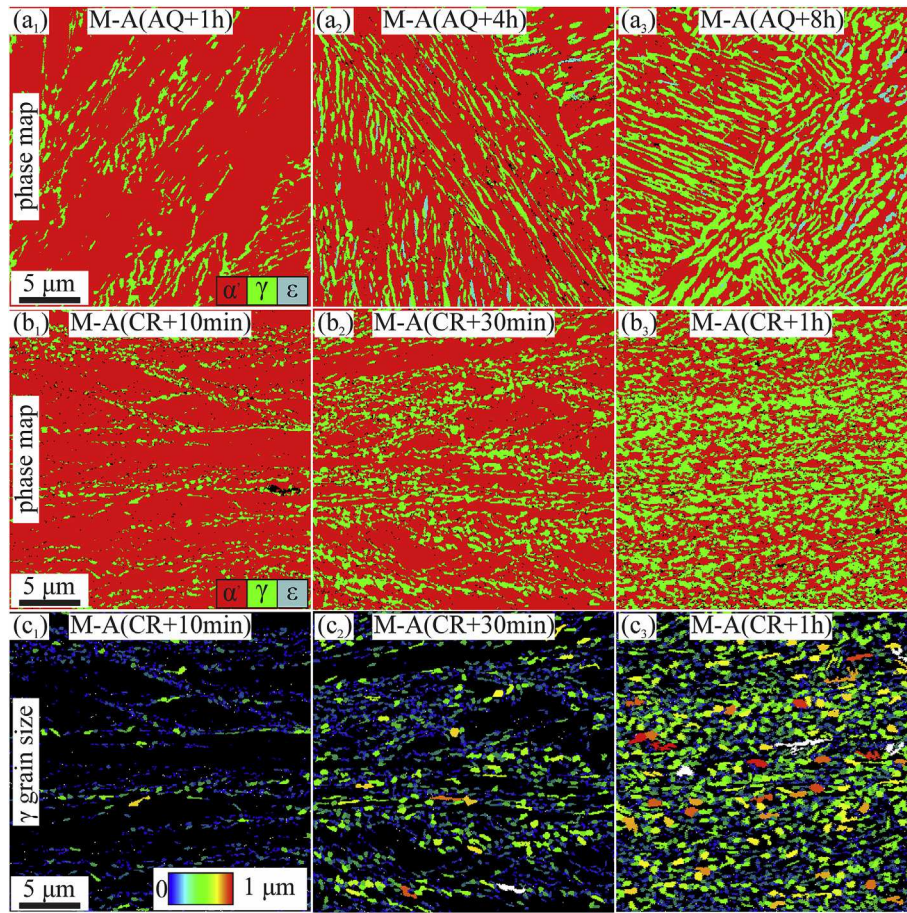


Fig. 3. (a) Phase maps for samples states (1) 1 h at 600 °C, $M-A_{(AQ+1h)}$; (2) 4 h at 600 °C, $M-A_{(AQ+4h)}$; (3) 8 h at 600 °C, $M-A_{(AQ+8h)}$. (b) Phase maps and (c) γ phase size maps for sample states (1) Cold rolled and 10 min at 600 °C, $M-A_{(CR+10min)}$; (2) Cold rolled and 30 min at 600 °C, $M-A_{(CR+30min)}$; (3) Cold rolled and 1 h at 600 °C, $M-A_{(CR+1h)}$, as characterized by EBSD measurements. $M-A_{(AQ+1h)}$: 600 °C 1 h annealed as-quenched martensite; $M-A_{(AQ+4h)}$: 600 °C 4 h annealed as-quenched martensite; $M-A_{(AQ+8h)}$: 600 °C 8 h annealed as-quenched martensite; $M-A_{(CR+10min)}$: 600 °C 10 min annealed cold-rolled martensite; $M-A_{(CR+30min)}$: 600 °C 30 min annealed cold-rolled martensite; $M-A_{(CR+1h)}$: 600 °C 1 h annealed cold-rolled martensite.

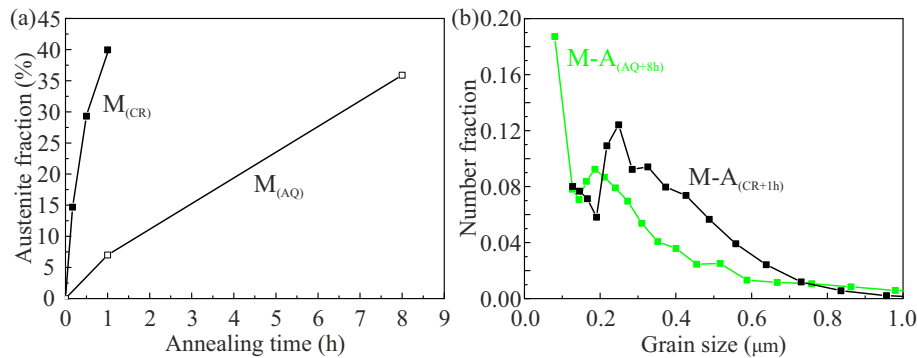


Fig. 4. (a) Evolution of reverted γ fraction during 600 °C annealing of cold-rolled α' martensite ($M_{(CR)}$) and as-quenched α' martensite ($M_{(AQ)}$); (b) Size distribution of reverted γ grains for 600 °C 8 h annealed as-quenched α' martensite $M-A_{(AQ+8h)}$ and 600 °C 1 h annealed cold-rolled α' martensite $M-A_{(CR+1h)}$. Note that the smallest γ grains might not be accurately indexed due to the limited spatial resolution of EBSD.

misorientations higher than 5° are excluded from the calculations. Here the KAM measure is used as an index for assessing accumulated plasticity in deformed γ grains [41].

3.3. Deformation micro-mechanisms

To understand the deformation micro-mechanisms associated

with the new thermo-mechanical treatment route, the microstructure evolution during deformation of $M-A_{(CR+1h)}$ is investigated next in detail. In our previous work, the internal structures of α' martensite and reverted γ in $M-A_{(AQ+8h)}$ were systematically characterized in detail by EBSD, TEM, ECCI and synchrotron X-ray diffraction (SXRD) analysis [4,5]. Due to the same annealing temperature applied to obtain $M-A_{(AQ+8h)}$ and $M-A_{(CR+1h)}$, i.e. 600 °C,

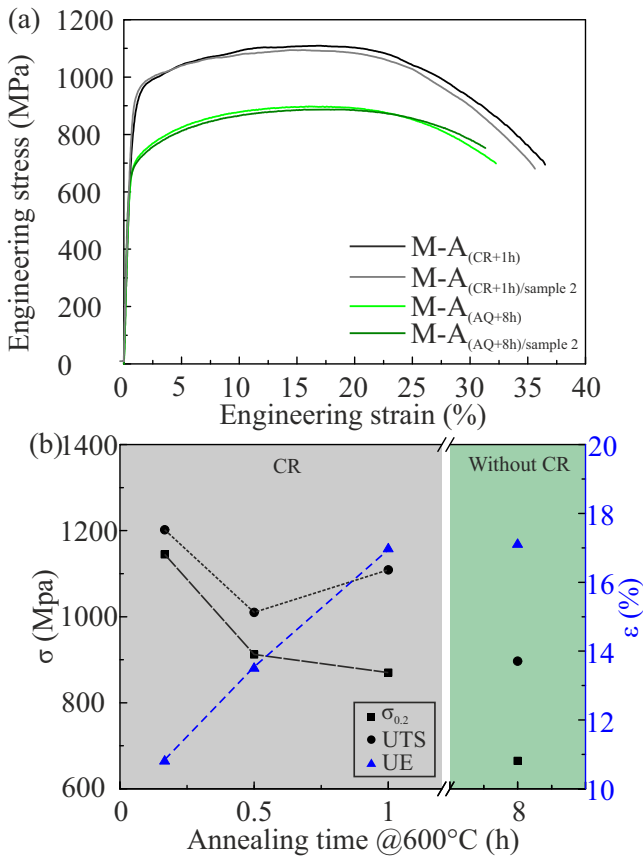


Fig. 5. (a) Engineering stress strain curves for samples M-A_(AQ+8h) and M-A_(CR+1h); (b) Mechanical property summary of sample M-A_(AQ+8h), sample M-A_(CR+10min), sample M-A_(CR+30min) and sample M-A_(CR+1h) in the undeformed state is also confirmed upon inspection of high resolution ECCI of reverted γ grains (see, e.g., yellow highlighted grains in Fig. 7). Based on the similarity of these sub-structural features and deformation mechanisms in sample M-A_(CR+1h), the characterization is carried out here mainly by ECCI, supported by EBSD based KAM and deformation texture analysis. The latter two methods are especially useful microstructure indicators since deformation in γ : (i) proceeds via multiplication of defects and thus increased lattice curvature due to deformation would be reflected as an increase in the KAM value; (ii) is accommodated by motion of dislocations, i.e. with $\langle 1-10 \rangle \{111\}$ slip systems, leading to a gradual build-up of $\{111\}$ //TA (tensile axis) texture.

reverted γ grains in both samples would assume the same chemical composition [5], e.g. similar stacking fault energy (SFE) [42,43]. Thus deformation of γ is expected to take place via activation of similar mechanisms, e.g. by formation of SFs, mechanical twinning and deformation-induced phase transformation [4,5].

Reverted γ grains in sample M-A_(AQ+8h) contain minor amounts of stacking faults (SFs) prior to deformation, which are growth faults during the reconstructive process. The formation of SFs in reverted γ grains in sample M-A_(CR+1h) in the undeformed state is also confirmed upon inspection of high resolution ECCI of reverted γ grains (see, e.g., yellow highlighted grains in Fig. 7). Based on the similarity of these sub-structural features and deformation mechanisms in sample M-A_(CR+1h), the characterization is carried out here mainly by ECCI, supported by EBSD based KAM and deformation texture analysis. The latter two methods are especially useful microstructure indicators since deformation in γ : (i) proceeds via multiplication of defects and thus increased lattice curvature due to deformation would be reflected as an increase in the KAM value; (ii) is accommodated by motion of dislocations, i.e. with $\langle 1-10 \rangle \{111\}$ slip systems, leading to a gradual build-up of $\{111\}$ //TA (tensile axis) texture.

We start with the undeformed state, where the microstructure of sample M-A_(CR+1h) consists of α' martensite (phase in red) and reverted γ grains (phase in green), as shown by the EBSD phase map in Fig. 7a₁. Reverted γ grains in sample M-A_(CR+1h), as

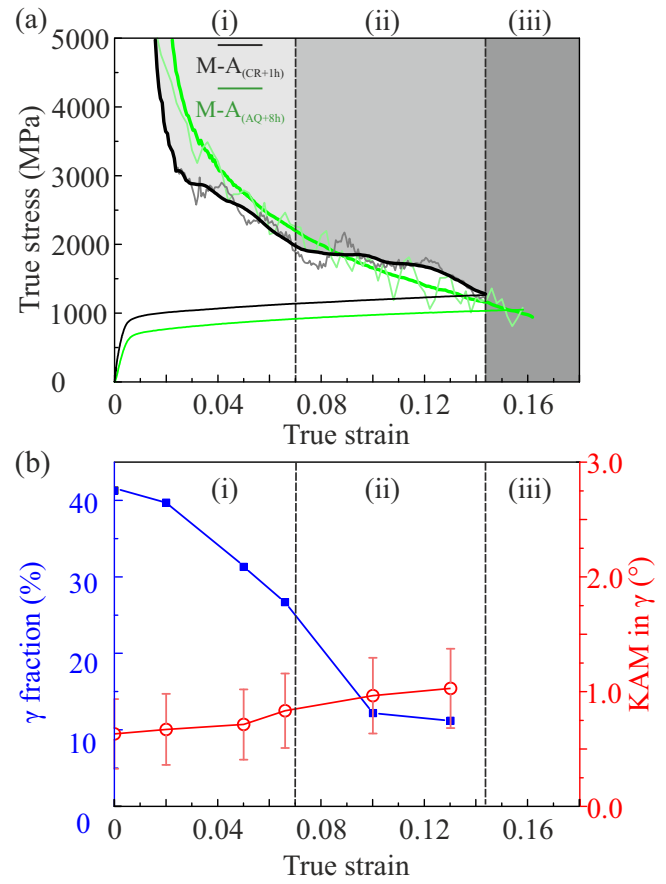


Fig. 6. (a) True stress strain curve and strain hardening curve for samples M-A_(AQ+8h) and M-A_(CR+1h); (b) Evolution of the γ fraction (blue data points) and kernel average misorientation (KAM) inside of the γ phase (red data points) during deformation of M-A_(CR+1h), as measured by EBSD. M-A_(AQ+8h): 600 °C 8 h annealed as-quenched martensite; M-A_(CR+1h): 600 °C 1 h annealed cold-rolled martensite. (For interpretation of the references to color in this figure legend, the reader is referred to the web version of this article.)

highlighted by yellow borders in Fig. 7a₂ and a₃, contain minor amounts of stacking faults (SFs) and do not inherit stored dislocations from the cold-rolled martensite. The α' martensite matrix is characterized by precipitates and dislocations (Fig. 7a₃).

During stage i, the early uniform deformation regime ($\epsilon < 0.07$), the strain hardening rate decreases after yielding, as shown by the black curve (Fig. 6a). About 15% of the γ grains transform into α' martensite and the remaining γ grains exhibit a slight increase in the KAM value up to $\epsilon = 0.05$ (Fig. 6b). Since an increase in the density of SFs is observed, it can be proposed that reverted γ grains are deformed by the motion of partial dislocations and multiplication of SFs (Fig. 7b₂–b₃). SFs within some of the γ grains are observed to be aligned along different orientations and thus divide γ grains into distinctly misoriented portions.

The deformation behavior in stage ii, the late uniform deformation regime, is characterized by the appearance of a strain hardening plateau between $\epsilon = 0.07$ and $\epsilon = 0.12$, followed by a decrease in strain hardening rate up to $\epsilon = 0.14$ (Fig. 6a). During stage ii, ~14.5% of the γ crystals transform into α' martensite and a continuous increase in KAM value in the remaining γ grains is observed (Fig. 6b). Thus, accompanying the significant activation of phase transformation, the remaining γ grains also exhibit pronounced plasticity. In fact, at the onset of the strain hardening

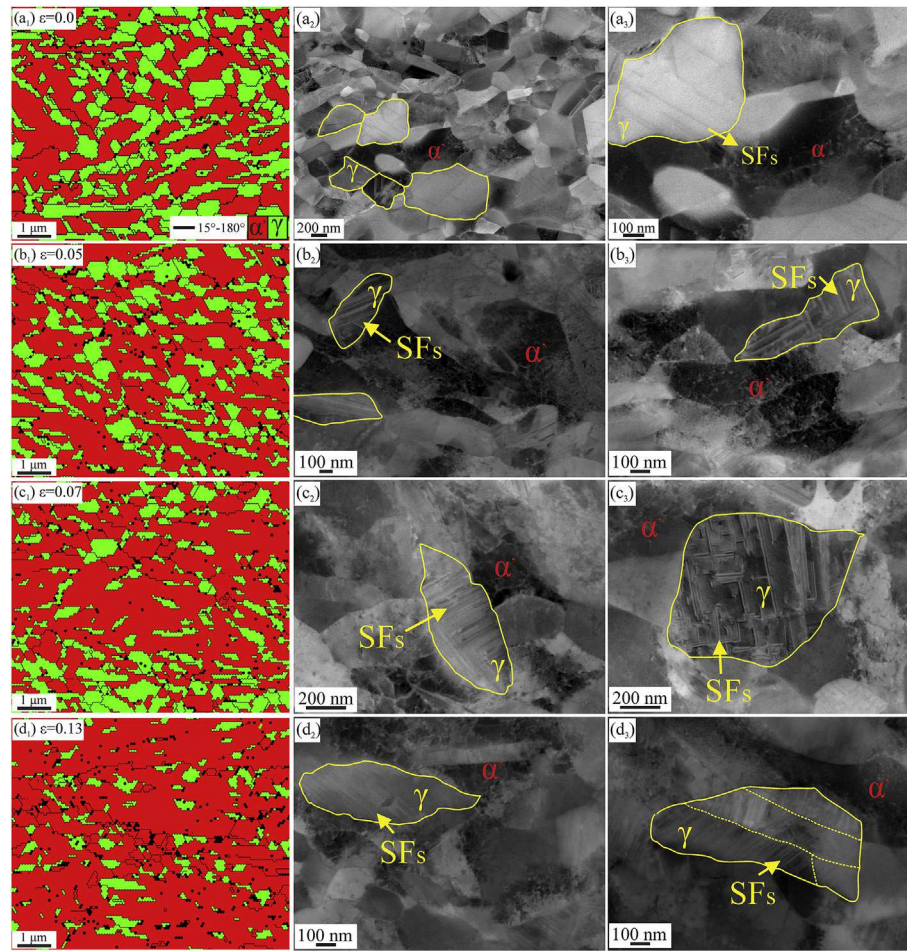


Fig. 7. Microstructure evolution during deformation of sample M-A_(CR+1h) at (a) $\varepsilon = 0$; (b) $\varepsilon = 0.05$; (c) $\varepsilon = 0.07$; (d) $\varepsilon = 0.13$, as characterized by (1) EBSD phase map; (2, 3) ECCI. M-A_(CR+1h): 600 °C 1 h annealed cold-rolled martensite.

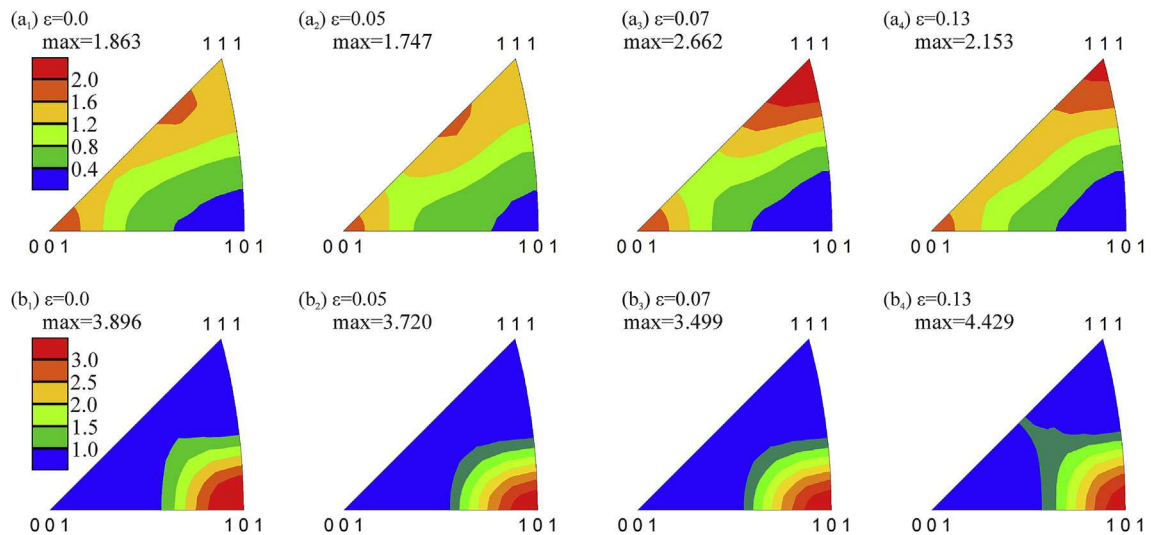


Fig. 8. IPF texture of M-A_(CR+1h) with respect to tensile axis for (a) γ and (b) martensite at (1) $\varepsilon = 0$; (2) $\varepsilon = 0.05$; (3) $\varepsilon = 0.07$; (4) $\varepsilon = 0.13$. M-A_(CR+1h): 600 °C 1 h annealed cold-rolled martensite.

plateau, i.e. at a strain of $\varepsilon = 0.07$ (Fig. 7c₂–c₃), γ grains are observed to contain denser SFs arrangements than at $\varepsilon = 0.05$ (Fig. 7b₂–b₃). This is also in accordance with the built-up of the $\{111\}$ //TA fiber

texture component in the remaining γ grains after straining to $\varepsilon = 0.07$ (Fig. 8a₁–a₃). The $\{111\}$ //TA fiber texture in γ is maintained during further straining (Fig. 8a₄). Meanwhile the martensite

generally maintains its $\{110\}$ /TA rolling texture during tensile deformation (Fig. 8b₁–b₄). Within the γ grains, a size-dependent deformation behavior in terms of size-dependent in-grain structures is observed (Fig. 7c₂, c₃). On the one hand, small γ grains tend to be deformed as a unit (Fig. 7c₂) while larger γ grains are generally deformed by building-up of a complex in-grain structure with several sets of SFs (Fig. 7c₃). On the other hand, the overall density of SFs within smaller γ grains is higher than that of larger γ grains, as observed e.g. by comparing Fig. 7c₃ with Fig. 7c₂. This size-dependent deformation behavior evolves with further straining. At $\epsilon = 0.13$, most small γ grains, in which no SFs can be resolved anymore, are transformed to α' martensite (Fig. 7d₂). In contrast, a large γ grain is observed to be densely covered by SFs in each segment, as indicated by the yellow dashed lines (Fig. 7d₃). Moreover, the in-grain contrast within one large γ grain indicates that each crystal portion has undergone deformation or phase transformation individually (Fig. 7d₃). The partial transformation behavior of large γ grains in sample M-A_(CR+1h), i.e. the observation that the large γ grain is first split into sub-grains and then each sub-grain transform individually, is in consistence with the observations made for sample M-A_(AQ+8h) [5].

4. Discussion

4.1. Influence of cold-rolling on microstructure evolution during reversion of martensite

In our previous work, the initial microstructure prior to reversion was as-quenched martensite, consisting of martensite packets, blocks and laths (Fig. 1a₁–a₂) [4]. These characteristic martensite grain boundaries do not exist in the microstructure anymore after cold rolling (~70% thickness reduction). In contrast, cold-rolled martensite contains numerous deformation-induced interfaces in the microstructure (Fig. 1b₁–b₂, Fig. 2) [29]. The difference in distribution of the martensite grain boundaries subsequently lead to different reversion processes in as-quenched martensite and cold-rolled martensite (Fig. 3). Comparing with low angle grain boundaries, reverted γ grains are preferentially formed along high angle grain boundaries during annealing at 600 °C, indicating shorter incubation time for γ formation along the high angle martensite grain boundaries (Fig. 3a₁–a₃, Fig. 3b₁–b₃). This is due to the low nucleation barrier for γ formation associated with grain boundaries carrying higher misorientation angles. They are characterized by higher tendency of elemental segregation and a higher martensite/martensite grain boundary energy [24,34,35]. Due to the existence of a bimodal distribution consisting of only high angle martensite grain boundaries (above 45°) and low angle martensite grain boundaries (below 15°) in as-quenched martensite, relatively long annealing times are required at 600 °C to form nano-sized interlath γ films along the majority of the lath martensite boundaries, e.g. 8 h (Fig. 3a₃). In contrast, due to the continuous misorientation distribution of the grain boundaries in cold-rolled martensite, a continuous nucleation and growth process is obtained, as indicated by the evolution of the γ grain size distribution in cold-rolled martensite (Fig. 3c₁–c₃) and quantitatively shown for samples M-A_(AQ+8h) and M-A_(CR+1h) (Fig. 4b). Eventually, a dispersed size distribution of γ grains is obtained in the cold rolled and heat treated sample M-A_(CR+1h) (Fig. 3c₃, Fig. 4b).

The growth of an γ nucleus is accompanied by elemental partitioning from martensite, and thus is controlled by the diffusion rate of corresponding elements across the martensite microstructure, [4,35,44]. Cold rolling enhances the diffusion rate due to high stored dislocation density [32,45,46] and thus results in a faster growth rate of reverted γ in cold-rolled martensite than in the as-quenched martensite, as observed when comparing the γ grain

size in sample M-A_(CR+1h) (Fig. 3b₃) with that in M-A_(AQ+1h) (Fig. 3a₁). Due to the existence of the high density of martensite grain boundaries and a high stored dislocation density, the combined high γ nucleation rate and growth kinetics in cold-rolled martensite lead to an accelerated reversion kinetics than as-quenched martensite (Fig. 4a).

To achieve the goal of enhancing the overall mechanical properties via the current thermo-mechanical treatment route, it is also essential to control the structure of the martensite. In this context, possible recrystallization of the cold-rolled martensite during annealing is undesired. Recrystallization proceeds by the formation of new strain-free grains and their growth consuming the deformed and recovered microstructure [47]. Thus, occurrence of recrystallization in cold-rolled martensite during annealing would lead to the loss of strength and of those microstructural features that are required as nucleation sites for the reversion. Previous works conducted on cold-rolled medium Mn steels reported that recrystallization in martensite leads to the formation of 'soft' ferrite during the reversion treatment [16,48,49]. During tensile testing, the yielding of 'soft' and almost dislocation-free ferrite leads to a discontinuous yielding behavior and to the appearance of Lüders bands on the tensile specimen's surface [16,48,49]. In the current cold-rolled martensite, recrystallization of martensite is suppressed due to precipitates and reverted γ grains (Fig. 7a₁–a₂), and a considerable density of low angle grain boundaries is preserved inside the martensite microstructure even after 600 °C isothermal annealing [50,51].

Given the scope of the presented work, a comparison to the field of grain boundary engineering (GBE) is relevant. GBE is based on quantitative characterization of grain boundaries with the aim of increasing fractions of special boundaries to improve grain boundary controlled properties [52–57]. For example, Schuh et al. pointed out the importance of grain boundary network topology in grain boundary engineering and established an experimental method to analyze the structure and topology of 2D grain boundary networks [52]. Bechtel et al. reported the increased resistance to hydrogen-induced intergranular embrittlement in metallic materials by increasing fractions of special grain boundaries [56]. For the martensitic boundaries of concern here such an approach is challenging due to the intrinsic complexity of lath martensite, see works of Morito et al. [38,58], as well as Morsdorf et al. [59]. Moreover, once the transformation takes place austenite grains are extremely fine in dimensions, thus they are often difficult to characterize. Luckily, the results presented here demonstrate that for martensitic matrix steels a strategy that is slightly simpler than present GBE efforts is sufficient. One apparently does not need to go as far as identifying property effects of specific boundaries, as long as one can introduce a wide collection of martensitic boundaries, which would help later in austenite reversion to lead to wide range of austenite stabilities. Our results show that the assessment of grain boundary misorientation on degree of segregation and nucleation energy is sufficient for the sought effect [60].

4.2. Mechanical properties and the associated deformation-mechanisms

Compared to M-A_(AQ+8h), M-A_(CR+1h) exhibits a higher yield stress $\sigma_{0.2}$, ultimate tensile stress UTS and maintained uniform elongation (Fig. 5). The yielding of the martensite-reverted γ microstructure occurs via yielding of the 'soft' phase γ crystals, which is influenced by the γ fraction, its deformation behavior and its stability [61]. Sample M-A_(AQ+8h) and sample M-A_(CR+1h) contain similar amounts of γ , e.g. 37 vol % for the former and 42 vol % for the latter. In either case, it is observed that γ is deformed by formation of SFs prior to deformation induced phase transformation (Fig. 7)

[4,5]. As reported by Sugimoto et al. [62], the stability of austenite is also influenced by the hydrostatic pressure from the surrounding second phase, e.g. a lower hydrostatic pressure would be exerted on retained austenite from ferrite than from bainite. Thus, higher hydrostatic pressure on γ is expected in sample M-A_(CR+1h) than in sample M-A_(AQ+8h), due to (i) the highly elastically strained lattice of cold-rolled martensite; and (ii) higher stored dislocation density after shorter time isothermal annealing. Therefore, due to the substantial ‘shielding’ effect from the surrounding martensite, a higher external stress is required in sample M-A_(CR+1h) to initiate deformation of γ grains, i.e. the yield stress is higher in sample M-A_(CR+1h).

The reasoning for enhanced ultimate tensile stress UTS, uniform elongation and strain hardening behavior in sample M-A_(CR+1h) are interlinked with each other and result from the interplay between the deformation and phase transformation processes in the microstructure. In the following, these processes will be analyzed in detail.

The strain hardening behavior of M-A_(CR+1h) is determined by the individual hardening behavior of martensite and γ , and their mutual strain partitioning behavior. The hardening of martensite arises from multiplication of dislocations and their interaction with precipitates. The hardening of reverted γ mainly contains two contributions, namely, strain hardening due to formation of SFs, and phase transformation into martensite, i.e. TRIP. In our previous work for sample state M-A_(AQ+8h) it was observed that martensite enters the plastic regime during the late stages of the uniform deformation, i.e. at $\epsilon > 0.05$. Here, due to the fact that martensite in M-A_(CR+1h) assumes much higher strength, it is expected that the contribution of martensite to strain hardening during the early uniform deformation regime (stage i) is not significant [18,48,63].

In the undeformed state, the microstructure of M-A_(CR+1h) consists of α' martensite and reverted γ (~42 vol %) (Fig. 6b). Preceding the transformation into α' martensite, the motion of partial dislocations and formation of SFs are observed in the γ grains (Fig. 7a2–a3).

During stage i, ~15 vol % γ transforms into α' martensite (Fig. 6b) and the remaining γ grains are only slightly deformed (Fig. 7b2–b3), i.e. only limited strengthening comes from the accumulated SFs within the remaining γ grains. The significant transformation of γ alone cannot cease the continuous decrease in strain hardening rate after yielding during stage i (Fig. 6a).

During stage ii, in addition to the significant amount of phase transformation, the remaining γ grains are also profoundly deformed, thus being able to terminate the decrease in strain hardening rate. This effect leads to the formation of a strain hardening plateau (Fig. 6a–b). The appearance of the strain hardening plateau is attributed to the dynamic strain partitioning process which arises from two factors, namely, (i) the orientation relationship between martensite and γ and (ii) the size effect of the transformation behavior of the γ crystals. On one hand, as a result of plastic deformation, a $\{111\}$ //TA texture is gradually built-up in γ crystals between $\epsilon = 0$ and $\epsilon = 0.07$ (Fig. 8a1–a3). Since martensite exhibits a $\{110\}$ //TA rolling texture (Fig. 8b1–b4), a gradual built-up of $\{111\}$ //TA texture in γ implies a progressive alignment of slip systems between martensite and γ , and thus an easier transfer of slip/plasticity from γ to martensite. This effect leads to improved deformation compatibility across the phase boundaries with ongoing deformation [64,65]. Thus, from $\epsilon = 0.07$ onwards, the contribution of martensite plasticity to the overall strain hardening becomes significant. On the other hand, a size-dependent deformation and transformation behavior exists within γ grains. While small γ grains tend to be deformed as a unit, large grains are preferentially divided into sub-grains and each sub-grain is deformed in an independent manner. At the same strain level, small

grains contain denser SFs than larger grains. Since SFs in deformed γ grains act as nucleation sites for α' martensite, deformed γ grains with sufficient accumulation of SFs would transform to α' martensite with further straining [5,66,67]. As a result, small γ grains transform into martensite already at relatively small strains and larger γ grains undergo partial phase transformation in a stepwise manner (Fig. 7b2–b3, c2–c3). The size effect on the mechanical stability of γ is consistent regarding previous results in sample state M-A_(AQ+8h) [5]. In addition, a high damage resistance is also preserved in sample M-A_(CR+1h) due to the high density of phase interfaces, i.e. deformation-induced martensite/tempered martensite interface, which act as high energy path for void nucleation, growth and coalescence processes [4]. Thus, the enhanced dynamic strain partitioning behavior and damage resistance give rise to an enhanced strain hardening behavior (Figs. 4b and 6a) and overall mechanical properties in sample M-A_(CR+1h) comparing with sample M-A_(AQ+8h).

5. Conclusions

We developed a new thermo-mechanical treatment route to render martensite ductile via spreading the micro-mechanical stability of reverted γ grains by widening the γ nucleation barrier in martensite. When annealed a microstructure consisting of γ grains with a wide dispersed size distribution and martensite is developed. This mechanism enables a spectral TRIP effect. The new thermo-mechanical treatment route leads to enhanced mechanical properties of the TRIP steel (Fe–9Mn–3Ni–1.4Al–0.01C, mass %). The main conclusions are:

- (1) Compared to as-quenched martensite, cold-rolled martensite (~70% thickness reduction) contains a higher density of martensite grain boundaries with a wide misorientation distribution.
- (2) The widened γ nucleation barrier in cold-rolled martensite results in a sequential nucleation and growth of γ grains during 600 °C annealing. Eventually, a microstructure consisting of martensite and γ grains with a wide dispersed size distribution is successfully obtained in the cold-rolled martensite and 600 °C 1 h annealed sample M-A_(CR+1h).
- (3) The wide size distribution of γ grains results in an active TRIP effect over a wide strain regime (spectral TRIP).
- (4) The proposed spectral TRIP strategy leads to yield stress $\sigma_{0.2}$ of 870 MPa, ultimate tensile stress UTS of 1110 MPa, uniform elongation of 19.2%, total elongation of 35% and enhanced strain hardening behavior in the cold-rolled and 600 °C 1 h annealed sample M-A_(CR+1h).

Acknowledgments

The authors gratefully acknowledge the funding by the European Research Council under the EU's 7th Framework Programme (FP7/2007–2013)/ERC Grant agreement 290998 “SmartMet”.

References

- [1] L. Yuan, D. Ponge, J. Wittig, P. Choi, J.A. Jiménez, D. Raabe, Nanoscale austenite reversion through partitioning, segregation and kinetic freezing: example of a ductile 2GPa Fe–Cr–C steel, *Acta Mater* 60 (2012) 2790–2804, <http://dx.doi.org/10.1016/j.actamat.2012.01.045>.
- [2] M. Kuzmina, D. Ponge, D. Raabe, Grain boundary segregation engineering and austenite reversion turn embrittlement into toughness: example of a 9wt.% medium Mn steel, *Acta Mater* 86 (2015) 182–192, <http://dx.doi.org/10.1016/j.actamat.2014.12.021>.
- [3] H. Springer, M. Belde, D. Raabe, Bulk combinatorial design of ductile martensitic stainless steels through confined martensite-to-austenite reversion, *Mat. Sci. Eng. A* 582 (2013) 235–244, <http://dx.doi.org/10.1016/>

- j.msea.2013.06.036.
- [4] M.-M. Wang, C.C. Tasan, D. Ponge, A.-C. Dippel, D. Raabe, Nanolaminate transformation-induced plasticity–twinning-induced plasticity steel with dynamic strain partitioning and enhanced damage resistance, *Acta Mater* 85 (2015) 216–228, <http://dx.doi.org/10.1016/j.actamat.2014.11.010>.
 - [5] M.-M. Wang, C.C. Tasan, D. Ponge, A. Kostka, D. Raabe, Smaller is less stable: size effects on twinning vs. transformation of reverted austenite in TRIP-maraging steels, *Acta Mater* 79 (2014) 268–281, <http://dx.doi.org/10.1016/j.actamat.2014.07.020>.
 - [6] M. Beldé, H. Springer, G. Inden, D. Raabe, Multiphase microstructures via confined precipitation and dissolution of vessel phases: example of austenite in martensitic steel, *Acta Mater* 86 (2015) 1–14, <http://dx.doi.org/10.1016/j.actamat.2014.11.025>.
 - [7] G.K. Tirumalasetty, M.A. van Huis, C. Kwakernaak, J. Sietsma, W.G. Sloof, H.W. Zandbergen, Deformation-induced austenite grain rotation and transformation in TRIP-assisted steel, *Acta Mater* 60 (2012) 1311–1321, <http://dx.doi.org/10.1016/j.actamat.2011.11.026>.
 - [8] Y. Tomota, H. Tokuda, Y. Adachi, M. Wakita, N. Minakawa, A. Moriai, et al., Tensile behavior of TRIP-aided multi-phase steels studied by in situ neutron diffraction, *Acta Mater* 52 (2004) 5737–5745, <http://dx.doi.org/10.1016/j.actamat.2004.08.016>.
 - [9] O. Muránsky, P. Sittner, J. Zrník, E.C. Oliver, In situ neutron diffraction investigation of the collaborative deformation–transformation mechanism in TRIP-assisted steels at room and elevated temperatures, *Acta Mater* 56 (2008) 3367–3379, <http://dx.doi.org/10.1016/j.actamat.2008.03.026>.
 - [10] S. Lee, B.C. De Cooman, On the selection of the optimal intercritical annealing temperature for medium Mn TRIP steel, *Metall. Mat. Trans. A* 44 (2013) 5018–5024, <http://dx.doi.org/10.1007/s11661-013-1860-2>.
 - [11] S.-J. Lee, S. Lee, B.C. De Cooman, Mn partitioning during the intercritical annealing of ultrafine-grained 6% Mn transformation-induced plasticity steel, *Scr. Mater* 64 (2011) 649–652, <http://dx.doi.org/10.1016/j.scriptamat.2010.12.012>.
 - [12] S. Lee, S.-J. Lee, B.C. De Cooman, Work hardening behavior of ultrafine-grained Mn transformation-induced plasticity steel, *Acta Mater* 59 (2011) 7546–7553, <http://dx.doi.org/10.1016/j.actamat.2011.08.030>.
 - [13] E. Paravicini Bagliani, M.J. Santofimia, L. Zhao, J. Sietsma, E. Anelli, Microstructure, tensile and toughness properties after quenching and partitioning treatments of a medium-carbon steel, *Mat. Sci. Eng. A* 559 (2013) 486–495, <http://dx.doi.org/10.1016/j.msea.2012.08.130>.
 - [14] M.J. Santofimia, L. Zhao, R. Petrov, C. Kwakernaak, W.G. Sloof, J. Sietsma, Microstructural development during the quenching and partitioning process in a newly designed low-carbon steel, *Acta Mater* 59 (2011) 6059–6068, <http://dx.doi.org/10.1016/j.actamat.2011.06.014>.
 - [15] E. De Moor, J.G. Speer, D.K. Matlock, J.-H. Kwak, S.-B. Lee, Effect of carbon and manganese on the quenching and partitioning response of CMnSi steels, *ISIJ Int.* 51 (2011) 137–144, <http://dx.doi.org/10.2355/isijinternational.51.137>.
 - [16] B.C. De Cooman, P. Gibbs, S. Lee, D.K. Matlock, Transmission electron microscopy analysis of yielding in ultrafine-grained medium Mn transformation-induced plasticity steel, *Metall. Mat. Trans. A* 44 (2013) 2563–2572, <http://dx.doi.org/10.1007/s11661-013-1638-6>.
 - [17] P.J. Gibbs, E. De Moor, M.J. Merwin, B. Clausen, J.G. Speer, D.K. Matlock, Austenite stability effects on tensile behavior of manganese-enriched-austenite transformation-induced plasticity steel, *Metall. Mat. Trans. A* 42 (2011) 3691–3702, <http://dx.doi.org/10.1007/s11661-011-0687-y>.
 - [18] J. Han, S.-J. Lee, J.-G. Jung, Y.-K. Lee, The effects of the initial martensite microstructure on the microstructure and tensile properties of intercritically annealed Fe–9Mn–0.05C steel, *Acta Mater* 78 (2014) 369–377, <http://dx.doi.org/10.1016/j.actamat.2014.07.005>.
 - [19] H. Luo, J. Shi, C. Wang, W. Cao, X. Sun, H. Dong, Experimental and numerical analysis on formation of stable austenite during the intercritical annealing of 5Mn steel, *Acta Mater* 59 (2011) 4002–4014, <http://dx.doi.org/10.1016/j.actamat.2011.03.025>.
 - [20] D.N. Hanlon, J. Sietsma, S. Van der Zwaag, The effect of plastic deformation of austenite on the kinetics of subsequent ferrite formation, *ISIJ Int.* 41 (2001) 1028–1036, <http://dx.doi.org/10.2355/isijinternational.41.1028>.
 - [21] H. Landheer, S.E. Offerman, R.H. Petrov, L.A.I. Kestens, The role of crystal misorientations during solid-state nucleation of ferrite in austenite, *Acta Mater* 57 (2009) 1486–1496, <http://dx.doi.org/10.1016/j.actamat.2008.11.034>.
 - [22] J. Sietsma, Phase transformations in steels, in: E. Pereloma, D.V. Edmonds (Eds.), *Phase Transform. Steels*, Woodhead Publishing, 2012, pp. 505–526, <http://dx.doi.org/10.1533/9780857096111.3.365>.
 - [23] P.J. Clemm, J.C. Fisher, The influence of grain boundaries on the nucleation of secondary phases, *Acta Metall.* 3 (1955) 70–73, [http://dx.doi.org/10.1016/0001-6160\(55\)90014-6](http://dx.doi.org/10.1016/0001-6160(55)90014-6).
 - [24] D. Raabe, S. Sandlöbes, J. Millán, D. Ponge, H. Assadi, M. Herbig, et al., Segregation engineering enables nanoscale martensite to austenite phase transformation at grain boundaries: a pathway to ductile martensite, *Acta Mater* 61 (2013) 6132–6152, <http://dx.doi.org/10.1016/j.actamat.2013.06.055>.
 - [25] N. Nakada, R. Fukagawa, T. Tsuchiyama, S. Takaki, D. Ponge, D. Raabe, Inheritance of dislocations and crystallographic texture during martensitic reversion into austenite, *ISIJ Int.* 53 (2013) 1286–1288.
 - [26] N. Nakada, T. Tsuchiyama, S. Takaki, D. Ponge, D. Raabe, Transition from diffusive to displacive austenite reversion in low-alloy steel, *ISIJ Int.* 53 (2013) 2275–2277.
 - [27] R.D.K. Misra, S. Nayak, P.K.C. Venkatasurya, V. Ramuni, M.C. Somani, L.P. Karjalainen, Nanograined/ultrafine-grained structure and tensile deformation behavior of shear phase reversion-induced 301 austenitic stainless steel, *Metall. Mat. Trans. A* 41 (2010) 2162–2174, <http://dx.doi.org/10.1007/s11661-010-0230-6>.
 - [28] S.-J. Lee, Y.-M. Park, Y.-K. Lee, Reverse transformation mechanism of martensite to austenite in a metastable austenitic alloy, *Mat. Sci. Eng. A* 515 (2009) 32–37, <http://dx.doi.org/10.1016/j.msea.2009.02.010>.
 - [29] H. Beladi, I.B. Timokhina, S. Mukherjee, P.D. Hodgson, Ultrafine ferrite formation through isothermal static phase transformation, *Acta Mater* 59 (2011) 4186–4196, <http://dx.doi.org/10.1016/j.actamat.2011.03.043>.
 - [30] S. Hossein Nedjad, M.N. Ahmadabadi, T. Furuhara, The extent and mechanism of nanostructure formation during cold rolling and aging of lath martensite in alloy steel, *Mat. Sci. Eng. A* 485 (2008) 544–549, <http://dx.doi.org/10.1016/j.msea.2007.08.008>.
 - [31] K. Ono, T.J. Koppenaal, The effects of prior deformation and transformations on the microstructure of an iron-nickel alloy, *Metall. Trans.* 5 (1974) 739–746, <http://dx.doi.org/10.1007/BF02644671>.
 - [32] R. Uejii, N. Tsuji, Y. Minamino, Y. Koizumi, Ultragrain refinement of plain low carbon steel by cold-rolling and annealing of martensite, *Acta Mater* 50 (2002) 4177–4189, [http://dx.doi.org/10.1016/S1359-6454\(02\)00260-4](http://dx.doi.org/10.1016/S1359-6454(02)00260-4).
 - [33] J.-L. Zhang, C.C. Tasan, M.L. Lai, J. Zhang, D. Raabe, Damage resistance in gum metal through cold work-induced microstructural heterogeneity, *J. Mat. Sci.* 1 (2015), <http://dx.doi.org/10.1007/s10853-015-9105-y>.
 - [34] D. Raabe, D. Ponge, O. Dmitrieva, B. Sander, Nanoprecipitate-hardened 1.5GPa steels with unexpected high ductility, *Scr. Mater* 60 (2009) 1141–1144, <http://dx.doi.org/10.1016/j.scriptamat.2009.02.062>.
 - [35] O. Dmitrieva, D. Ponge, G. Inden, J. Millán, P. Choi, J. Sietsma, et al., Chemical gradients across phase boundaries between martensite and austenite in steel studied by atom probe tomography and simulation, *Acta Mater* 59 (2011) 364–374, <http://dx.doi.org/10.1016/j.actamat.2010.09.042>.
 - [36] Z. Zhao, M. Ramesh, D. Raabe, A.M. Cuitiño, R. Radovitzky, Investigation of three-dimensional aspects of grain-scale plastic surface deformation of an aluminum oligocrystal, *Int. J. Plast.* 24 (2008) 2278–2297, <http://dx.doi.org/10.1016/j.ijplas.2008.01.002>.
 - [37] D. Raabe, M. Sachtleber, Z. Zhao, F. Roters, S. Zaefferer, Micromechanical and macromechanical effects in grain scale polycrystal plasticity experimentation and simulation, *Acta Mater* 49 (2001) 3433–3441, [http://dx.doi.org/10.1016/S1359-6454\(01\)00242-7](http://dx.doi.org/10.1016/S1359-6454(01)00242-7).
 - [38] S. Morito, H. Tanaka, R. Konishi, T. Furuhara, T. Maki, The morphology and crystallography of lath martensite in Fe–C alloys, *Acta Mater* 51 (2003) 1789–1799, [http://dx.doi.org/10.1016/S1359-6454\(02\)00577-3](http://dx.doi.org/10.1016/S1359-6454(02)00577-3).
 - [39] S. Morito, Y. Adachi, T. Ohba, Morphology and crystallography of sub-blocks in ultra-low carbon lath martensite steel, *Mat. Trans.* 50 (2009) 1919–1923, <http://dx.doi.org/10.2320/matertrans.MRA2008409>.
 - [40] S.I. Wright, M.M. Nowell, D.P. Field, A review of strain analysis using electron backscatter diffraction, *Microsc. Microanal.* 17 (2011) 316–329.
 - [41] M. Calcagnotto, D. Ponge, E. Demir, D. Raabe, Orientation gradients and geometrically necessary dislocations in ultrafine grained dual-phase steels studied by 2D and 3D EBSD, *Mat. Sci. Eng. A* 527 (2010) 2738–2746, <http://dx.doi.org/10.1016/j.msea.2010.01.004>.
 - [42] T.-H. Lee, E. Shin, C.-S. Oh, H.-Y. Ha, S.-J. Kim, Correlation between stacking fault energy and deformation microstructure in high-interstitial-alloyed austenitic steels, *Acta Mater* 58 (2010) 3173–3186, <http://dx.doi.org/10.1016/j.actamat.2010.01.056>.
 - [43] T. Masumura, N. Nakada, T. Tsuchiyama, S. Takaki, T. Koyano, K. Adachi, The difference in thermal and mechanical stabilities of austenite between carbon- and nitrogen-added metastable austenitic stainless steels, *Acta Mater* 84 (2015) 330–338, <http://dx.doi.org/10.1016/j.actamat.2014.10.041>.
 - [44] J. Millán, S. Sandlöbes, A. Al-Zubi, T. Hickel, P. Choi, J. Neugebauer, et al., Designing heusler nanoprecipitates by elastic misfit stabilization in Fe–Mn maraging steels, *Acta Mater* 76 (2014) 94–105, <http://dx.doi.org/10.1016/j.actamat.2014.05.016>.
 - [45] X. Huang, S. Morito, N. Hansen, T. Maki, Ultrafine structure and high strength in cold-rolled martensite, *Metall. Mat. Trans. A Phys. Metall. Mat. Sci.* 43 (2012) 3517–3531, <http://dx.doi.org/10.1007/s11661-012-1275-5>.
 - [46] H.F. Lan, W.J. Liu, X.H. Liu, Ultrafine ferrite grains produced by tempering cold-rolled martensite in low carbon and microalloyed Steels, *ISIJ Int.* 47 (2007) 1652–1657, <http://dx.doi.org/10.2355/isijinternational.47.1652>.
 - [47] F.J. Humphreys, Recovery after deformation, in: F.J. Humphreys, M. Hatherly (Eds.), *Recryst. Relat. Annealing Phenom.*, second ed., Elsevier, Oxford, 2004, pp. 169–213 doi:<http://dx.doi.org/10.1016/B978-008044164-1/50010-4>.
 - [48] P.J. Gibbs, B.C. De Cooman, D.W. Brown, B. Clausen, J.G. Schroth, M.J. Merwin, et al., Strain partitioning in ultra-fine grained medium-manganese transformation induced plasticity steel, *Mat. Sci. Eng. A* 609 (2014) 323–333, <http://dx.doi.org/10.1016/j.msea.2014.03.120>.
 - [49] R. Sun, W. Xu, C. Wang, J. Shi, H. Dong, W. Cao, Work hardening behavior of ultrafine grained duplex medium-mn steels processed by ART-annealing, *Steel Res. Int.* 83 (2012) 316–321, <http://dx.doi.org/10.1002/srin.201100317>.
 - [50] D. Raabe, On the orientation dependence of static recovery in low-carbon steels I, *Scr. Metall. Mater* 33 (1995) 735–740.
 - [51] D. Raabe, Investigation of the orientation dependence of recovery in low-carbon steel by use of single orientation determination, *Steel Res.* 66 (1995) 222–229.

- [52] C.A. Schuh, M. Kumar, W.E. King, Analysis of grain boundary networks and their evolution during grain boundary engineering, *Acta Mater* 51 (2003) 687–700, [http://dx.doi.org/10.1016/S1359-6454\(02\)00447-0](http://dx.doi.org/10.1016/S1359-6454(02)00447-0).
- [53] P. Lejček, S. Hofmann, V. Paidar, Solute segregation and classification of [100] tilt grain boundaries in α -iron: consequences for grain boundary engineering, *Acta Mater* 51 (2003) 3951–3963, [http://dx.doi.org/10.1016/S1359-6454\(03\)00219-2](http://dx.doi.org/10.1016/S1359-6454(03)00219-2).
- [54] V. Randle, Twinning-related grain boundary engineering, *Acta Mater* 52 (2004) 4067–4081, <http://dx.doi.org/10.1016/j.actamat.2004.05.031>.
- [55] V. Randle, G. Owen, Mechanisms of grain boundary engineering, *Acta Mater* 54 (2006) 1777–1783, <http://dx.doi.org/10.1016/j.actamat.2005.11.046>.
- [56] S. Bechtle, M. Kumar, B.P. Somerday, M.E. Launey, R.O. Ritchie, Grain-boundary engineering markedly reduces susceptibility to intergranular hydrogen embrittlement in metallic materials, *Acta Mater* 57 (2009) 4148–4157, <http://dx.doi.org/10.1016/j.actamat.2009.05.012>.
- [57] S. Sinha, D.-I. Kim, E. Fleury, S. Suwas, Effect of grain boundary engineering on the microstructure and mechanical properties of copper containing austenitic stainless steel, *Mat. Sci. Eng. A* 626 (2015) 175–185, <http://dx.doi.org/10.1016/j.msea.2014.11.053>.
- [58] S. Morito, X. Huang, T. Furuhara, T. Maki, N. Hansen, The morphology and crystallography of lath martensite in alloy steels, *Acta Mater* 54 (2006) 5323–5331, <http://dx.doi.org/10.1016/j.actamat.2006.07.009>.
- [59] L. Morsdorf, C.C. Tasan, D. Ponge, D. Raabe, 3D structural and atomic-scale analysis of lath martensite: effect of the transformation sequence, *Acta Mater* 95 (2015) 366–377, <http://dx.doi.org/10.1016/j.actamat.2015.05.023>.
- [60] D. Raabe, M. Herbig, S. Sandlöbes, Y. Li, D. Tytko, M. Kuzmina, et al., Grain boundary segregation engineering in metallic alloys: a pathway to the design of interfaces, *Curr. Opin. Solid State Mat. Sci.* 18 (2014) 253–261, <http://dx.doi.org/10.1016/j.cossms.2014.06.002>.
- [61] M.A. Zaccane, G. Krauss, Elastic limits and microplastic response in ultrahigh strength carbon steels, *Metall. Trans. A* 20 (1989) 188–191, <http://dx.doi.org/10.1007/BF02647507>.
- [62] K. Sugimoto, M. Masahiro, Second phase morphology on retained austenite morphology and tensile properties in a TRIP-aided dual-phase steel Sheet, *ISIJ Int.* 33 (1993) 775–782.
- [63] Q. Han, Y. Kang, P.D. Hodgson, N. Stanford, Quantitative measurement of strain partitioning and slip systems in a dual-phase steel, *Scr. Mater* 69 (2013) 13–16, <http://dx.doi.org/10.1016/j.scriptamat.2013.03.021>.
- [64] P. Wang, N. Xiao, S. Lu, D. Li, Y. Li, Investigation of the mechanical stability of reversed austenite in 13%Cr–4%Ni martensitic stainless steel during the uniaxial tensile test, *Mat. Sci. Eng. A* 586 (2013) 292–300, <http://dx.doi.org/10.1016/j.msea.2013.08.028>.
- [65] J. Luster, M.A. Morris, Compatibility of deformation in two-phase Ti–Al alloys: dependence on microstructure and orientation relationships, *Metall. Mat. Trans. A* 26 (1995) 1745–1756, <http://dx.doi.org/10.1007/BF02670762>.
- [66] M.A. Jaswon, Mechanism of phase transformations in metals, *Nature* 177 (1956) 419–421.
- [67] G.B. Olson, M. Cohen, A general mechanism of martensitic nucleation: Part II. FCC–BCC and other martensitic transformations, *Metall. Trans. A* 7A (1976) 1905–1914.
- [68] J.K. Mackenzie, Second paper on statistics associated with the random disorientation of cubes, *Biometrika* 45 (1958) 229–240, <http://dx.doi.org/10.2307/2333059>.